High-Field-Effect Mobility of Low-Crystallinity Conjugated Polymers with Localized Aggregates

Sung Y. Son,[†,§] Yebyeol Kim,[†,§] Junwoo Lee,[†] Gang-Young Lee,[†] Won-Tae Park,[‡] Yong-Young Noh,[‡] Chan E. Park,*[,†] and Taiho Park*[,†]

[†]Department of Chemical Engineering, Pohang University of Science and Technology, San 31, Nam-gu, Pohang, Gyeongbuk 790-780, Korea

[‡]Department of Energy and Materials Engineering, Dongguk University, 30, Pildong-ro 1-gil, Jung-gu, Seoul 04620, Korea

Ⓢ Supporting Information

ABSTRACT: Charge carriers typically move faster in crystalline regions than in amorphous regions in conjugated polymers because polymer chains adopt a regular arrangement resulting in a high degree of $\pi-\pi$ stacking in crystalline regions. In contrast, the random polymer chain orientation in amorphous regions hinders connectivity between conjugated backbones; thus, it hinders charge carrier delocalization. Various studies have attempted to enhance charge carrier transport by increasing crystallinity. However, these approaches are inevitably limited by the semicrystalline nature of conjugated polymers. Moreover, high-crystallinity conjugated polymers have proven inadequate for soft electronics applications because of their poor mechanical resilience. Increasing the polymer chain connectivity by forming localized aggregates via π-orbital overlap among several conjugated backbones in amorphous regions provides a more effective approach to efficient charge carrier transport. A simple strategy relying on the density of random copolymer alkyl side chains was developed to generate these localized aggregates. In this strategy, steric hindrance caused by these side chains was modulated to change their density. Interestingly, a random polymer exhibiting low alkyl side chain density and crystallinity displayed greatly enhanced field-effect mobility $(1.37\ \text{cm}^2/(\text{V·s}))$ compared with highly crystalline poly(3-hexylthiophene).
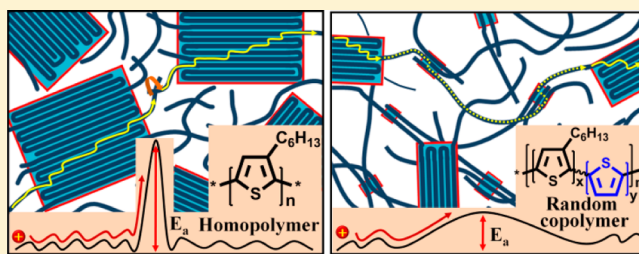
INTRODUCTION

Various conjugated polymers (CPs) have found use in organic field-effect transistor (OFET) applications because of their tunable electronic properties, solution processability, and applicability to soft electronics.[1−13] Most CPs form complicated microstructures combining crystalline and amorphous domains due to their semicrystalline nature. This heterogeneity has significantly affected the performance of resulting OFETs.[14−18]

Polymer chains in crystalline domains adopt a regular packing resulting in a high degree of π-orbital overlap between backbones.[19] In contrast, this π-orbital overlap is limited in amorphous domains because of random polymer chain orientation that can allow a substantial degree of freedom in side chains leading to restricted close packing. These differences in chain packing and π-orbital overlap facilitate charge carrier transport in crystalline domains but hinder it in amorphous areas. Moreover, a considerable number of polymer chains may act as dead ends for charge carrier transport in amorphous domains.

Several attempts at increasing CP crystallinity have been made to enhance charge carrier mobility in OFETs.[20,21] However, these approaches are inevitably stalled because of the semicrystalline nature of CPs. Even the best-known high-crystallinity poly(3-hexylthiophene) (P3HT) has shown a limited level of crystallinity.[22,23] In addition, high crystallinity affects mechanical resilience, which is unsuitable for soft electronics applications.[24] Therefore, one might think that an increase in charge carrier transport in amorphous areas is more reasonable and effective for high field-effect mobility in OFETs and soft electronics applications. Recently, a high-mobility CP exhibiting low crystallinity has shown the possibility of this approach.[25,26]

In the charge transport behavior in most CPs, intrachain transport is much faster than interchain charge transport.[27,28] However, high-mobility in OFETs cannot be achieved without the aid of appropriate interchain charge hopping despite facilitated charge transport along the backbone. Therefore, charge carrier transport hinges on connectivity enhancement between chains via π-orbital overlap as well as a high degree of backbone planarity regardless of crystallinity. Thanks to such an enhancement, charge carriers are expected to move along the increased pathways and bypass unpredictable energetic trap sites, especially in amorphous regions, reducing the average activation energy (E_a) for charge carrier transport.

It has been suggested that localized aggregates formed by π-orbital overlap can increase interchain charge carrier trans-

port.[29] They can act as charge transport junctions between conjugated backbones (Figure 1a), effectively enhancing charge
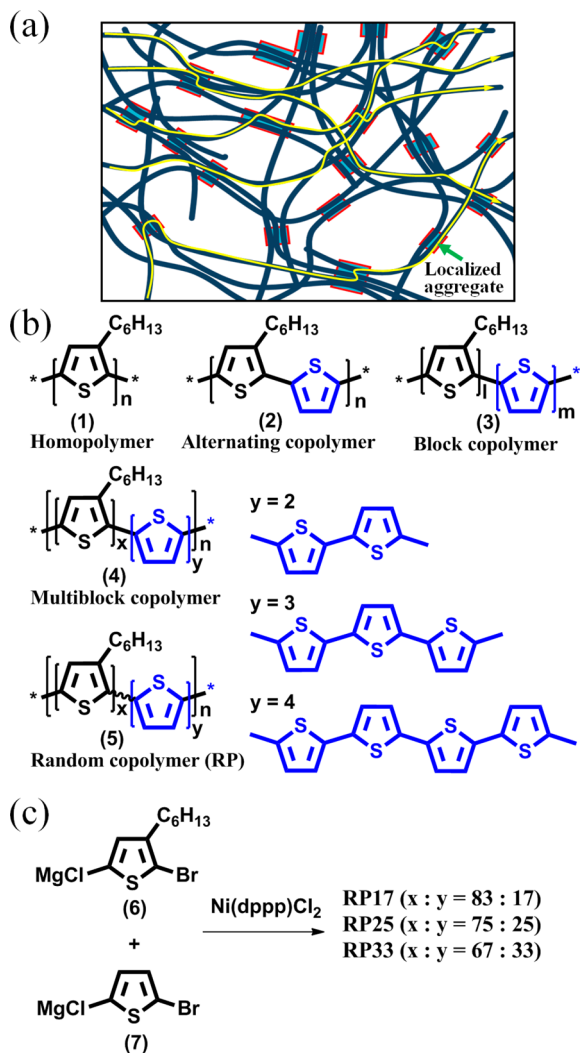

Figure 1. (a) Schematic illustration of a microstructure comprising highly interconnected polymer chains via localized aggregates. Yellow arrows represent possible charge carrier pathways. (b) Chemical structures of the P3HT homopolymer (1) and alternating (2), block (3), multiblock (4), and random 3-hexylthiophene−thiophene copolymers (5, $y \geq 2$). (c) Synthetic scheme for **RP17**, **RP25**, and **RP33**.

carrier delocalization in amorphous regions. However, systematic molecular design should be required to achieve microstructures containing such unconventional localized aggregates. The design of CPs needs to account for the bulkiness of side chains on the conjugated backbone. Most CPs bear bulky solubilizing side chains, which may significantly interfere with face-to-face packing and consequently π-orbital overlap between conjugated backbones.[30] Small side chains that give a minimum level of solubility to polymers are preferred for close chain packing[31] but do not ensure formation of localized aggregates.

Various types of polymers may form depending on monomer composition (1−5, Figure 1b). The introduction of several successive pendant-free units (for $y \geq 2$, Figure 1b) into polymer chains is most likely to give microstructures containing localized aggregates because of their higher propensity to

produce close chain packing than monomers bearing side chains due to the reduced steric hindrance caused by side chains. Multiblock (4) and random copolymers (5) can incorporate these units in patches. While such multiblock copolymers are technically very difficult and time-consuming to synthesize, their random analogues may be obtained by chain-growth polymerization if the comonomers present similar reactivity.[32,33]

Polythiophene derivatives have been extensively used as model polymers because their microstructures and optoelectronic properties are tunable using several parameters such as molecular weights,[34−38] side chains,[39−41] and regioregularity.[42−44] In this study, a series of polythiophene-based random copolymers (RPs) were synthesized and introduced in devices to evaluate the existence of localized aggregates and the effectiveness of charge carrier transport despite low crystallinity.

Interestingly, the RP exhibiting the lowest degree of crystallinity achieved the highest field-effect mobility (1.37 cm²/(V·s)). This mobility corresponds to the highest value obtained from thiophene-based CPs to the best of our knowledge (P3HT has shown a maximum field-effect mobility of 0.49 cm²/(V·s)).[45]

Herein, P3HT and a series of RPs were compared to determine the effects of structural regularity on microstructures. Furthermore, all polymer microstructures were systematically studied to assess their relationship with charge carrier transport in OFETs.

■ RESULTS AND DISCUSSION

Synthesis and Characterization. After a Grignard metathesis (GRIM) polymerization[46] at room temperature (see details in the Supporting Information), copolymerization of 2-bromo-5-chloro-magnesio-3-hexylthiophene (**6**) and 2-bromo-5-chloro-magnesiothiophene (**7**) with thiophene ratios of 17, 25, and 33 mol % afforded **RP17**, **RP25**, and **RP33**, respectively (Figure 1c). Table 1 lists the polymerization information for P3HT and RPs along with their thermal and absorption properties. Actual thiophene molar compositions amounted to 21, 28, and 33 mol % for **RP17**, **RP25**, and **RP33**, respectively, calculated from the integration values of peaks from aromatic protons on hexylthiophene (6.95−7.04 ppm) and thiophene (7.04−7.15 ppm) moieties. This slight discrepancy from monomer feed ratios may result from a difference in comonomer reactivity caused by the hexyl substituent. As intended, number-average molecular weights (M_n) equaled 16.0 kg/mol with a polydispersity index (M_w/M_n) ranging between 1.06 and 1.15 (Figure S1), which is essential to avoid molecular weight effects on optoelectronic properties and formation of microstructures.

The chemical structures of P3HT and RPs were investigated by ¹H NMR spectroscopy (Figure S2). This evaluation focused on the 6.93−7.18 ppm range because the incorporation of thiophene units usually brings significant changes in this aromatic region (Figure 2a). P3HT showed one strong regioregular peak at 6.98 ppm and one weak regioirregular peak at 7.00 ppm, indicative of its high regioregularity.[47] It is noticed that the regioregularity of P3HT, **RP17**, **RP25**, and **RP33** was 94.6%, 93%, 90.2%, and 89.6%, respectively. These values were obtained from the peaks between 2.5 and 3.0 ppm (Figure S3).[35,47] In contrast, **RP17** exhibited several new peaks (b−e, Figure 2a) ascribed to incorporation of one thiophene unit between two hexyl thiophene units. The intensity of these peaks increased with increasing thiophene ratio, indicating the

Table 1. Polymerization Information and Thermal and Absorption Properties of P3HT, RP17, RP25, and RP33

| polymer | polymerization[a] | | thermal properties[e] | | | absorption properties[i] | | | | | | | film energetics |
| | thiophene (mol %) | $M_n{}^c$ (kg/mol) | $T_m{}^f$ (°C) | $T_c{}^g$ (°C) | $H_f{}^h$ (J/g) | in CHCl₃ | | in toluene | | film (after annealing)[l] | | | |
						$\lambda_{max}{}^j$ (nm)	$\lambda_{edge}{}^k$ (nm)	$\lambda_{max}{}^j$ (nm)	$\lambda_{edge}{}^k$ (nm)	$\lambda_{max}{}^j$ (nm)	$\lambda_{edge}{}^k$ (nm)	$\Delta E_{gap}{}^m$ (eV)	HOMO[n] (eV)
P3HT	0	16.0 (1.06)[d]	218	188	15.3	454	535	458	537	547	636	1.95	4.92
RP17	17 (21)[b]	16.0 (1.07)[d]	171	137	9.89	463	544	462	545	545	635	1.95	4.91
RP25	25 (28)[b]	16.0 (1.10)[d]	147	103	6.82	469	549	469	550	544	636	1.95	4.91
RP33	33 (33)[b]	16.0 (1.15)[d]	123	92	4.64	470	552	486	634	543	635	1.95	4.92

[a]The polymerization was conducted in a glovebox at room temperature. [b]Actual thiophene content in the polymer. [c]Number-average molecular weights measured by gel permeation chromatography (GPC). [d]Polydispersity indices measured by GPC. [e]Characterized by differential scanning calorimetry (DSC) at heating and cooling rates of 10 °C/min. [f]Melting temperature. [g]Recrystallization temperature. [h]Enthalpy of fusion calculated by integrating the endothermic peak in the DSC thermogram. [i]Characterized by UV−vis absorption. [j]Absorption maximum. [k]Absorption edge. [l]Prepared by spin-coating a 15 mg/mL solution in chloroform on a glass substrate at 3000 rpm for 30 s before annealing for 10 min at 200, 150, 120, and 100 °C for P3HT, RP17, RP25, and RP33, respectively. [m]Calculated as $\Delta E_{gap} = (1240/\lambda_{edge})$. [n]Highest occupied molecular orbital (HOMO) determined from the onset oxidation potentials of the corresponding polymer using cyclic voltammetry (vs Fc/Fc⁺) in film state (Figure S4). The lowest unoccupied molecular orbital (LUMO) values for the polymers can be estimated from the corresponding HOMO and ΔE_{gap} values.
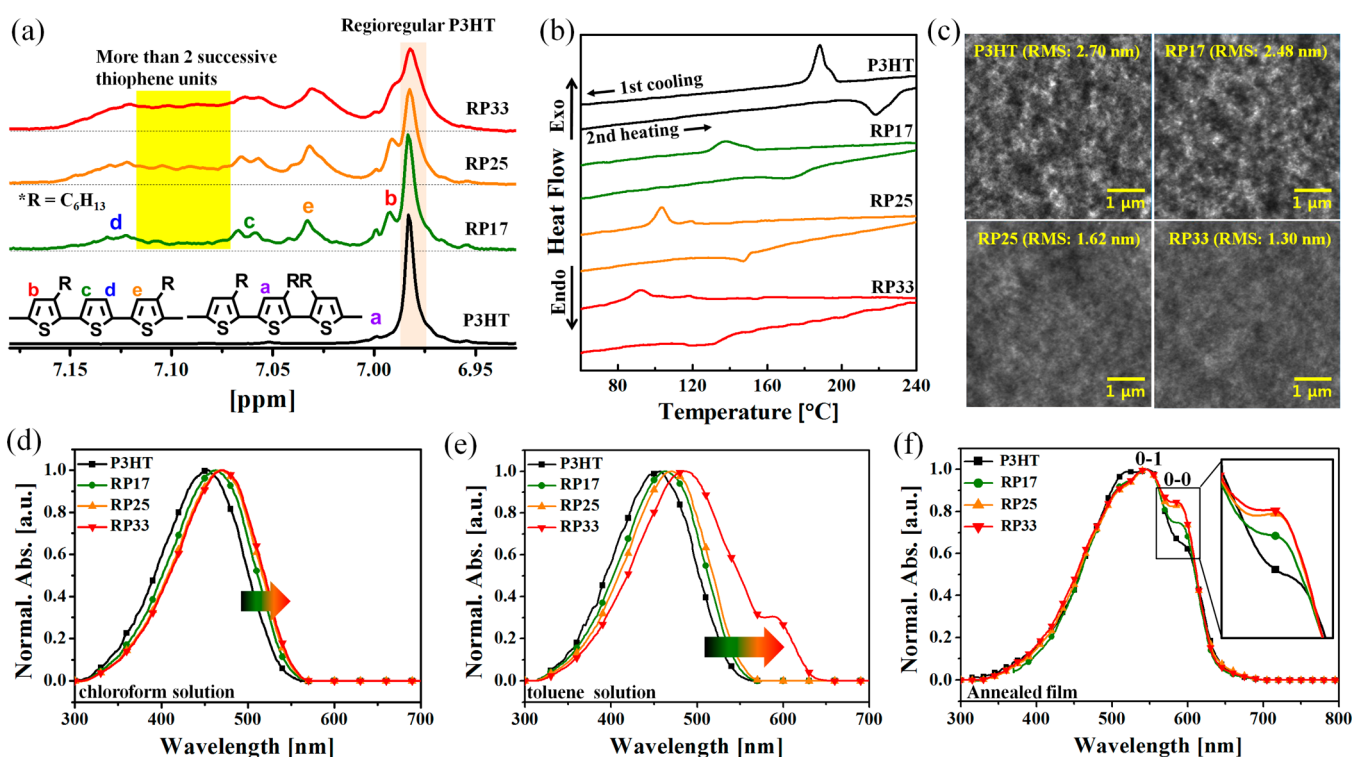

Figure 2. (a) ¹H NMR spectra between 6.93 and 7.18 ppm. (b) DSC thermograms. (c) Tapping mode AFM images. Normalized UV−vis absorption spectra of (d) chloroform solution, (e) toluene solution, and (f) annealed films.

statistical existence of both repeating units in the polymer chains. Moreover, broad peaks were observed between 7.07 and 7.12 ppm (yellow box, Figure 2a), consistent with the presence of more than two successive thiophene units in **RP17**, **RP25**, and **RP33**. For thiophene oligomers, proton peaks for the central units appear between those of their terminal analogues.[48−50] These broad peaks grow when the thiophene content increases because the probability for one thiophene unit to bind another rises.

Crystallinity Analysis. All polymers were investigated by differential scanning calorimetry (DSC). These measurements provide information on intermolecular interaction and crystallinity. P3HT displayed melting (T_m) and recrystallization temperatures (T_c) at 218 and 188 °C, corresponding to endothermic and exothermic processes, respectively (Table 1

and Figure 2b). The T_m and T_c values gradually decreased with increasing thiophene content for RPs implying decreased intermolecular interaction between polymer chains due to the reduced structural regularity. This phenomenon was also associated with a drop in enthalpy of fusion (ΔH_f) (Table 1), suggesting that structural regularity of polymer chains directly affected the crystallinity.

A similar tendency was observed by atomic force microscopy (AFM) (Figure 2c, see Figure S5 for the enlarged images). P3HT exhibited a rough surface (RMS = 2.70 nm). Meanwhile, **RP25** showed a smooth surface (RMS = 1.62 nm), implying a considerably reduced crystallinity.[51,52] **RP33** presented an even smoother surface (RMS = 1.30 nm) than **RP25**. These results indicate that crystallinity gradually decreases with increasing thiophene content in the conjugated backbone. Therefore,
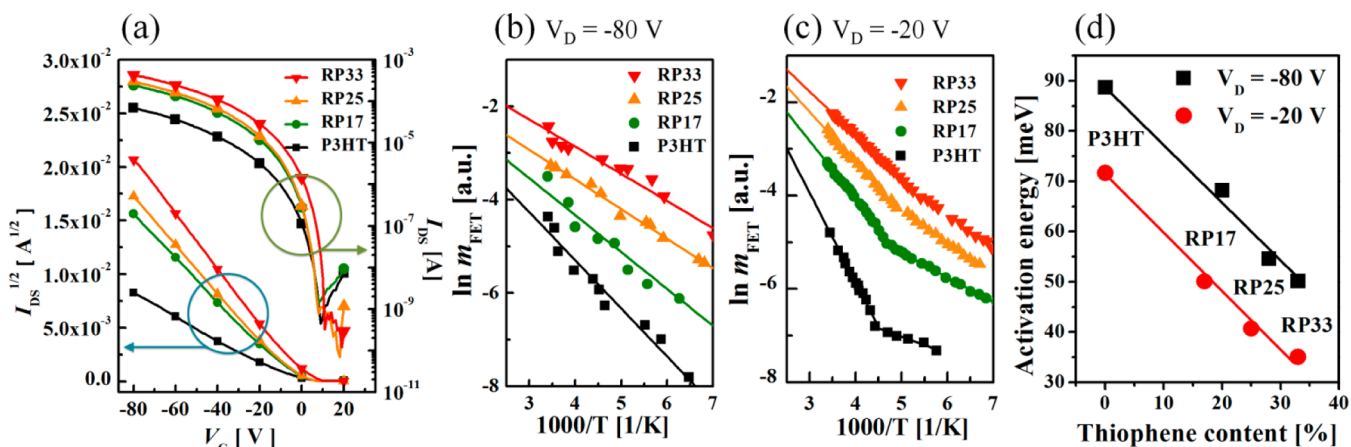
Figure 3. (a) Transfer characteristics at a fixed V_{drain} (V_D) of −80 V for OFETs using annealed polymer films. (b, c) Temperature dependence of polymer field-effect mobilities at a V_D of −80 and −20 V, respectively. (d) Calculated activation energies at a V_D of −80 and −20 V. The activation energy at V_D = −20 V was calculated in the high temperature regime (>226 K).

Table 2. OFET Characteristics and Structural Features

| | | | | | | | structural features[e] | | | |
| | organic field effect transistor (OFET) characteristics[a] | | | | | | out-of-plane direction | | in-plane direction | |
polymer	E_a[b]	μ_{avg}[c] (cm²/(V·s))	μ_{high}[d] (cm²/(V·s))	on/off ratio	V_{th} (V)	V_{on} (V)	SS	100[f] [Å]	$\pi-\pi$[f] [Å]	100[f] [Å]	$\pi-\pi$[f] [Å]
P3HT	71.6	0.17	0.19	2×10^5	−5.4	9	2.3	16.34		16.9	3.84
RP17	50.1	0.88	0.9	2×10^5	−4.5	8	2.1	16.34	3.77	16.55	3.71
RP25	40.7	0.93	0.94	4×10^5	−4.7	8	1.8	15.74	3.77, 3.63	16.55	3.71
RP33	35.1	1.31	1.37	10×10^5	0	11	0.8	14.77	3.63	15.89	

[a]Polymer solutions in chloroform were spin-coated on octadecyltrichlorosilane-modified substrates to yield 20 nm thick films. Their OFET characteristics were obtained in the saturation region (drain voltage = −80 V) for annealed OFETs. [b]Activation energy for charge carrier transport calculated using eq 1, $\mu = \mu_0 \exp(-E_a/(kT))$. [c]Average field-effect mobilities are calculated from 17 individual OFETs. [d]Optimal hole mobility. [e]Measured by 2D-GIWAXS. [f]Obtained using $q_z = (4\pi \sin \theta)/\lambda$ and $2d \cdot \sin \theta = n\lambda$, where n is a positive integer, λ is the incident wavelength, and θ is the scattering angle.

DSC and AFM results show that the statistical existence of thiophene units in the polymer chains significantly impacts intermolecular interaction and crystallinity. **RP33** exhibited the lowest crystallinity despite its least sterically hindered chains associated with the dramatic decrease in hexyl side chain density. This indicates that side chain density and structural irregularity influence molecular−molecular interaction to a greater extent than steric hindrance.

Optical Properties. The packing behaviors of P3HT and RPs in solution and films were investigated using UV−vis absorption spectroscopy since packing modes affect the optical properties of conjugated polymers. Obtained absorption properties are summarized in Table 1. Absorption spectra presented a gradual red shift in chloroform (Figure 2d) and chlorobenzene (Figure S6a) when the thiophene content increased. All absorption maxima (λ_{max}) and edges (λ_{edge}) shifted to higher wavelengths. This suggests an increase in the effective conjugation length of the polymer backbone, which is highly related to backbone planarity in solution state. The role of thiophene units in the planarization of the polymer backbone was studied by density functional theory at the B3LYP/6-31G(d,p) level using four different thiophene oligomers (Figure S7). In the model for P3HT (case 1), the dihedral angles Φ_1 and Φ_2 between three central thiophene rings amounted to 33.6° and 32.9°, respectively. When the number of thiophene units increased from one to three, the dihedral angles gradually decreased (case 2: $\Phi_1 = 36°$, $\Phi_2 = 16.4°$; case 3: $\Phi_1 = 17.6°$, $\Phi_2 = 23.4°$; case 4: $\Phi_1 = 19°$, $\Phi_2 = 17°$) because of the reduced

steric hindrance in the absence of hexyl side chains. This result agrees well with the absorption properties of P3HT and RPs in chloroform and chlorobenzene.

Absorption spectra presented a similar bathochromic behavior in toluene (Figure 2e). Interestingly, the absorption spectrum of **RP33** in toluene exhibited a distinct shoulder peak around 600 nm. A shoulder peak typically appears on the right side of a main peak (at a higher wavelength) when conjugated polymers form aggregates in solution.[32] This shoulder peak indicates that **RP33** polymer chains tend to form aggregates in toluene because of their lower solubility in this solvent than in chloroform or chlorobenzene. These **RP33** aggregates may originate from the facilitated $\pi-\pi$ interactions between conjugated backbones because of the enhanced degree of backbone planarity and closer face-to-face packing caused by the reduced density of hexyl side chains and steric hindrance in solution state.

In addition, the solid-state packing of P3HT and RPs and the annealing effects on their microstructures were evaluated by UV−vis absorption spectroscopy using as-cast and annealed films. All as-cast films generated almost identical spectra, indicative of their similar packing mode (Figure S6b). In contrast, annealed films presented clear differences between shoulder peaks around 600 nm (Figure 2f). F. C. Spano et al. described that increase in the 0−0/0−1 absorption ratio indicates enhanced intrachain exciton coupling.[53] In the absorption spectra of annealed films, the ratio gradually increased with increasing thiophene content. This implies
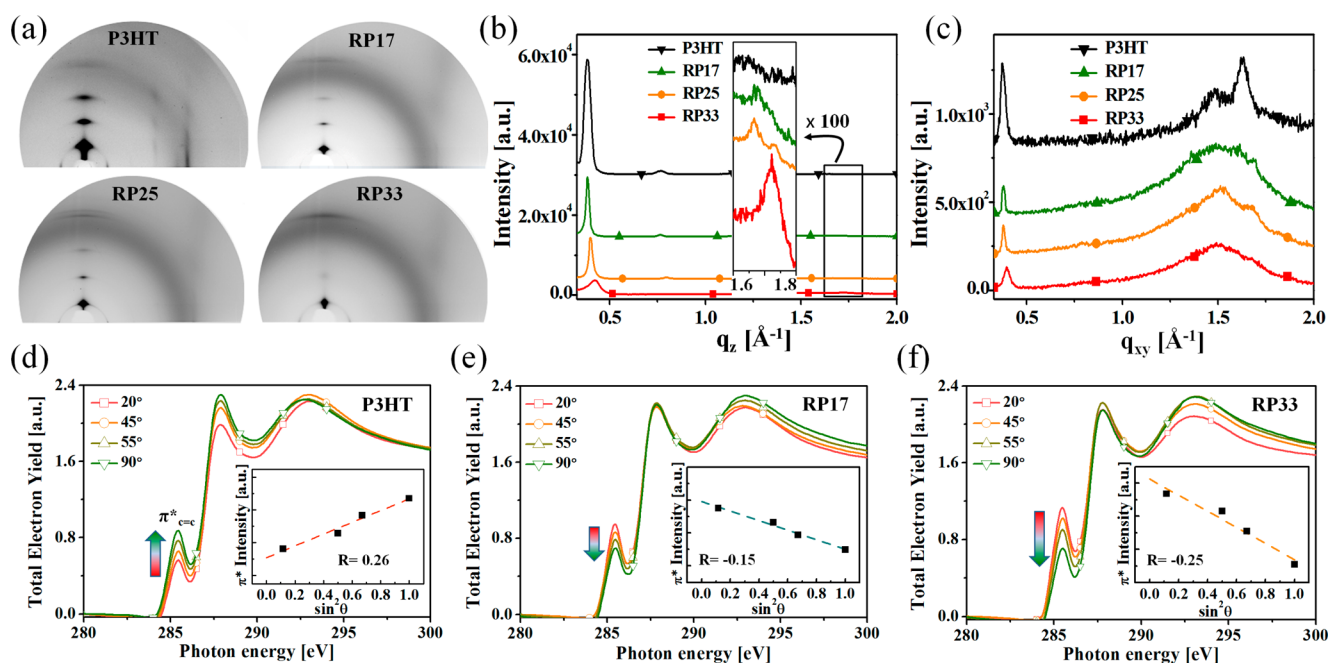
Figure 4. (a) Two-dimensional GIWAXS patterns. (b) Out-of-plane and (c) in-plane XRD spectra extracted from 2D-GIWAXS data. Inset of panel b shows a magnified portion of the spectra between 1.6 and 1.8q_z. NEXAFS spectra of (d) P3HT, (e) **RP17**, and (f) **RP33** at multiple incidence angles. Insets of panels d−f show π^* intensity as a function of $\sin^2 \theta$.

that intrachain exciton delocalization was facilitated due to the planarization of backbones in RPs as shown in the optical properties in solution state and the DFT calculation.

OFET Characteristics. We preliminarily investigated the output curves to observe contact resistance between polymer and source/drain (Au) electrodes (Figure S8). The good linear and saturation behavior with negligible contact resistance indicated the well-matched highest occupied molecular orbital (HOMO) energy values of the polymers with work-function of Au (Table 1 and Figure S4).

The charge transport properties of as-cast (Figure S9) and annealed films (Figure 3a) of P3HT, **RP17**, **RP25**, and **RP33** were investigated at room temperature. All OFET parameters of as-cast and annealed films are summarized in Table S2 and Table 2, respectively. In the case of the as-cast OFETs, all field-effect mobilities were similar, but after thermal annealing, the mobility values were increased and varied. This indicates that thermodynamically stable chain conformation was obtained by thermal annealing. Consequently, other parameters were altered.

After thermal annealing, RPs with higher thiophene content exhibited higher OFET performance (Table 2). In particular **RP33**, which showed the lowest degree of crystallinity, presented approximately seven times higher field-effect mobility (1.37 cm^2/(V·s)) than high-crystallinity P3HT (0.19 cm^2/(V·s)). This may result from the increased backbone planarity as observed by UV−vis absorption spectroscopy that could facilitate charge transport along the backbone. Meanwhile, we also consider that their morphological difference could play an important role in the highly improved field-effect mobility in company with the increased backbone planarity.[25,54] Systematic morphology study should be followed to investigate charge transport behavior in **RP33**.

The subthreshold (SS) character of OFETs numerically accounts for the amount of trap sites in the channel region. CPs inevitably contain numerous trap sites caused by structural and energetic disorder in amorphous regions. **RP33** exhibited a steep SS of 0.8 V per decade compared with P3HT, indicating a low trap density in the channel region.[55] In contrast, increasing the hexylthiophene content caused the SS value to rise, consistent with the higher prevalence of traps when the device was turned on. Moreover, the threshold voltage (V_{th}) was positively shifted, suggesting a reduced trap density in accordance with the increase in thiophene content.[56] These results indicate that a low degree of energetic disorder can be obtained even though the degree of structural disorder is high.

Since an average E_a for charge carrier transport more obviously represents the energetic disorder of a CP, temperature effects on the field-effect mobility of as-prepared OFETs were evaluated at the high (−80 V) and low (−20 V) drain voltage region (Figure 3b,c) to determine the E_a. The charge carrier transport of OFETs is usually assessed using the Arrhenius equation:

$$\mu = \mu_0 \exp(-E_a/(kT)) \tag{1}$$

where k is the Boltzmann constant and T is the absolute temperature.[57,58] The temperature-dependent mobilities of P3HT and RPs matched the Arrhenius relationship, suggesting that charge carrier transport occurs by thermal activation hopping, which is limited in amorphous regions. P3HT exhibited a distinct transition temperature of the slope around 226 K at the low (−20 V) drain voltage (Figure 3c). The two different activation energies indicated that there is a great energy offset between the ordered crystal and disordered amorphous regions.[59] The energy offset diminished with increasing thiophene content, consistent with the reduced crystallinity observed by DSC and AFM. Furthermore, the both activation energies measured at the high (−80 V) and low (−20 V) drain voltages linearly decreased with increasing thiophene content (Figure 3d), suggesting that higher content of thiophene in RPs facilitated charge transport despite the increased structural disorder.

Morphology Study. Charge carrier transport strongly depends on microstructure in CPs. To explain the decrease in E_a for charge carrier transport with increasing thiophene content, all polymer films were characterized by two-dimensional grazing incidence wide-angle X-ray scattering (2D-GIWAXS) (Figure 4a).

The 2D-GIWAXS pattern of P3HT displayed strong out-of-plane (h00) peaks, indicative of well-ordered, long-range lamellar structures. It also showed a distinct in-plane (010) peak representing in-plane π–π stacking induced by the predominant edge-on orientation of backbones in crystallites. The intensity of both peaks diminished with increasing thiophene content, consistent with the reduced crystallinity observed by DSC and AFM. Furthermore, the decrease in crystallinity was clearly observed both in azimuthal X-ray scans on the out-of-plane (100) reflections (Figure S10) and correlation lengths[60] estimated from full width at half-maximum (fwhm) of out-of-plane (100) reflections (Figure S11 and Table S3) indicating that structural irregularity inhibited regular and long-range chain ordering.

All peak intensities diminished with increasing thiophene content, except for the out-of-plane (010) peak corresponding to out-of-plane π–π stacking. The behavior of this (010) peak was clearer in XRD spectra extracted from 2D-GIWAXS data (Figure 4b,c). While this (010) peak was hardly detected in the magnified XRD spectrum of P3HT, its equivalent for **RP17** was observed at 1.67 Å^{-1} at low intensity. Interestingly, **RP25** exhibited two (010) peaks, implying the existence of two different π–π stacking modes. These peaks appeared at the same q_z values (1.67 and 1.73 Å^{-1}) as for **RP17** and **RP33**, respectively, suggesting that **RP25** generated an intermediate microstructure between those of **RP17** and **RP33**. **RP33** displayed the strongest (010) peak, indicating that it adopted the highest degree of out-of-plane π–π stacking.

In-plane spectra presented considerably weaker (100) peaks than their out-of-plane counterparts, implying that crystallites mainly followed an edge-on orientation. In general, out-of-plane (010) peaks are associated with in-plane (h00) peaks ascribed to crystallites adopting a face-on orientation. However, the opposite was observed in this study. This suggests that the out-of-plane (010) peak did not originate from crystallites formed by a combination of edge-to-edge and face-to-face packing but from localized aggregates produced via π–π stacking. These localized aggregates could readily form in **RP33** because of the enhanced backbone planarity and the incorporated successive thiophene units, which exhibit much reduced steric hindrance compared with hexyl thiophene units. Furthermore, they are expected to play a very important role in interchain charge hopping in the microstructure of low-crystallinity **RP33**.

In addition, as listed in Table 2, the diminution of d-spacings and π–π stacking distance with increasing thiophene content promotes charge carrier transport. This stems from the decrease in steric hindrance in the absence of certain hexyl side chains. As mentioned above, crystallites in all the polymers predominantly adopted an edge-on orientation. However, 2D-GIWAXS showed that localized aggregates lay flat on the substrate with out-of-plane π–π stacking. Since these aggregates were expected to form by a short-range π–π stacking of polymer chains in amorphous regions, their orientation probably depended on that of polymer chains in these regions.

The near-edge X-ray absorption fine structure (NEXAFS) technique provides information on the average conformation of polymer chains in a film by detecting the X-ray absorption in chemical combinations, such as π-orbital, single bond, and double bond.[61] The intensity of the carbon–carbon 1s → π^* resonance pattern at 285.4 eV is proportional to the squared dot product of π^* vector of the polymer chain and incident beam according to Fermi's Golden Rule.[62] The dichroic ratio R, which represents an average chain conformation of films, was calculated using

$$R = (I_{90°} - I_{0°})/(I_{90°} + I_{0°}) \tag{2}$$

where $I_{90°}$ and $I_{0°}$ are intensities at incident angles of 90° and 0°, respectively.[63] An R value of zero indicates a wholly random orientation for each polymer chain, while values of −1 and 0.7 correspond to perfect face-on and edge-on orientations, respectively.[62]

Polymer films were characterized using NEXAFS to validate 2D-GIWAXS results (Figures 4d–f and S12). P3HT exhibited an edge-on average orientation of polymer chains (R = 0.26). In contrast, R values amounted to −0.15, −0.16, and −0.25 for **RP17**, **RP25**, and **RP33**, respectively, consistent with a face-on orientation. Interestingly, RPs adopted an overall face-on chain orientation although their crystallites mainly presented an edge-on orientation. In RPs (especially **RP33**), the predominantly face-on polymer chains in amorphous regions formed localized aggregates via out-of-plane π–π stacking.

In CPs, charge carriers need to properly move from one conjugated backbone to another at places where conjugation break occurs for facilitating overall charge carrier transport. In general, interchain charge transport favorably happens in crystalline domains in CPs like P3HT because polymer chains adopt a regular packing. However, it is significantly limited in amorphous regions due to the poor interconnectivity between conjugated backbones (Figure 5a).[64] Therefore, an average E_a for charge carrier transport in amorphous regions is substantially higher than that in the crystalline domains. Conversely, low-crystallinity **RP33** exhibited enhanced backbone planarity and microstructures containing unconventional localized aggregates formed via out-of-plane π–π stacking between polymer chains in an amorphous matrix. Thanks to the two features the average E_a for charge carrier transport was effectively reduced in **RP33** and consequently both intra- and interchain charge transport were significantly facilitated despite its low crystallinity (Figure 5b).

■ CONCLUSION

A strategy was developed to improve the charge carrier transport of conjugated polymers. This strategy involved increasing connectivity between polymer chains by forming localized aggregates in amorphous regions. A series of RPs were synthesized using different monomer feed ratios to control the density of hexyl side chains, which play an important role in molecular–molecular interaction. The crystallinity decreased with the reduction of the side chains density concomitant with the increase in structural irregularity. Interestingly, **RP33**, which exhibited the lowest crystallinity, showed a greatly enhanced field-effect mobility compared with the high-crystallinity P3HT, reaching 1.37 cm^2/(V·s). This enhancement is attributed to the increased backbone planarity and the existence of localized aggregates in amorphous regions, giving rise to enhanced intra- and interchain charge transport, respectively. These results open the door to novel approaches to next-generation
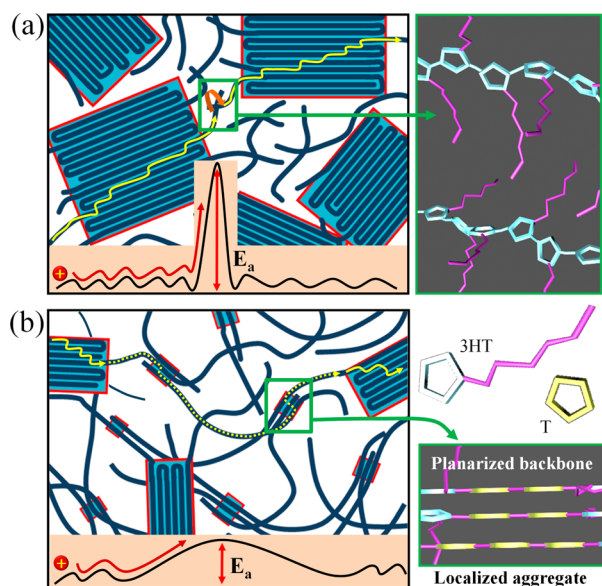
Figure 5. Schematic representations of (a) a P3HT-type microstructure exhibiting high crystallinity and poor interconnectivity in amorphous regions and (b) an **RP33**-type microstructure presenting low crystallinity and great interconnectivity via localized aggregates in amorphous regions. Yellow arrows represent charge carrier pathways. Insets: activation energies of charge carrier transport for each microstructure.

conjugated polymers exhibiting low E_a for charge carrier transport.

■ ASSOCIATED CONTENT

Ⓢ Supporting Information

The Supporting Information is available free of charge on the ACS Publications website at DOI: 10.1021/jacs.6b01046.

> Experimental details, synthesis of polymers, device fabrication, and detailed experimental procedures (PDF)

■ AUTHOR INFORMATION

Corresponding Authors

*taihopark@postech.ac.kr
*cep@postech.ac.kr

Author Contributions

§S.S. and Y.K. contributed equally.

Notes

The authors declare no competing financial interest.

■ ACKNOWLEDGMENTS

■ REFERENCES

(1) Sirringhaus, H.; Tessler, N.; Friend, R. H. *Science* **1998**, *280*, 1741−1744.

(2) Ong, B. S.; Wu, Y.; Liu, P.; Gardner, S. *J. Am. Chem. Soc.* **2004**, *126*, 3378−3379.

(3) Li, Y.; Wu, Y.; Liu, P.; Birau, M.; Pan, H.; Ong, B. S. *Adv. Mater.* **2006**, *18*, 3029−3032.

(4) McCulloch, I.; Heeney, M.; Bailey, C.; Genevicius, K.; Macdonald, I.; Shkunov, M.; Sparrowe, D.; Tierney, S.; Wagner, R.; Zhang, W.; Chabinyc, M. L.; Kline, R. J.; McGehee, M. D.; Toney, M. F. *Nat. Mater.* **2006**, *5*, 328−333.

(5) Guo, X.; Kim, F. S.; Jenekhe, S. A.; Watson, M. D. *J. Am. Chem. Soc.* **2009**, *131*, 7206−7207.

(6) Zhang, M.; Tsao, H. N.; Pisula, W.; Yang, C.; Mishra, A. K.; Müllen, K. *J. Am. Chem. Soc.* **2007**, *129*, 3472−3473.

(7) Fong, H. H.; Pozdin, V. A.; Amassian, A.; Malliaras, G. G.; Smilgies, D. M.; He, M.; Gasper, S.; Zhang, F.; Sorensen, M. *J. Am. Chem. Soc.* **2008**, *130*, 13202−13203.

(8) Zhang, W.; Smith, J.; Watkins, S. E.; Gysel, R.; McGehee, M.; Salleo, A.; Kirkpatrick, J.; Ashraf, S.; Anthopoulos, T.; Heeney, M.; McCulloch, I. *J. Am. Chem. Soc.* **2010**, *132*, 11437−11439.

(9) Lei, T.; Cao, Y.; Fan, Y.; Liu, C. J.; Yuan, S. C.; Pei, J. *J. Am. Chem. Soc.* **2011**, *133*, 6099−6101.

(10) Ashraf, R. S.; Kronemeijer, A. J.; James, D. I.; Sirringhaus, H.; McCulloch, I. *Chem. Commun.* **2012**, *48*, 3939−3941.

(11) Lee, J.; Han, A. R.; Kim, J.; Kim, Y.; Oh, J. H.; Yang, C. *J. Am. Chem. Soc.* **2012**, *134*, 20713−20721.

(12) Li, J.; Zhao, Y.; Tan, H. S.; Guo, Y.; Di, C. A.; Yu, G.; Liu, Y.; Lin, M.; Lim, S. H.; Zhou, Y.; Su, H.; Ong, B. S. *Sci. Rep.* **2012**, *2*, 754.

(13) Kim, G.; Kang, S. J.; Dutta, G. K.; Han, Y. K.; Shin, T. J.; Noh, Y. Y.; Yang, C. *J. Am. Chem. Soc.* **2014**, *136*, 9477−9483.

(14) Sirringhaus, H.; Brown, P. J.; Friend, R. H.; Nielsen, M. M.; Bechgaard, K.; Langeveld-Voss, B. M. W.; Spiering, A. J. H.; Janssen, R. A. J.; Meijer, E. W.; Herwig, P.; de Leeuw, D. M. *Nature* **1999**, *401*, 685−688.

(15) Kim, D. H.; Park, Y. D.; Jang, Y.; Yang, H.; Kim, Y. H.; Han, J. I.; Moon, D. G.; Park, S.; Chang, T.; Chang, C.; Joo, M.; Ryu, C. Y.; Cho, K. *Adv. Funct. Mater.* **2005**, *15*, 77−82.

(16) Kline, R. J.; McGehee, M. D.; Toney, M. F. *Nat. Mater.* **2006**, *5*, 222−228.

(17) Kang, I.; Yun, H. J.; Chung, D. S.; Kwon, S. K.; Kim, Y. H. *J. Am. Chem. Soc.* **2013**, *135*, 14896−14899.

(18) Lee, J.; Han, A. R.; Yu, H.; Shin, T. J.; Yang, C.; Oh, J. H. *J. Am. Chem. Soc.* **2013**, *135*, 9540−9547.

(19) Kim, Y.; Cook, S.; Tuladhar, S. M.; Choulis, S. A.; Nelson, J.; Durrant, J. R.; Bradley, D. D. C.; Giles, M.; McCulloch, I.; Ha, C. S.; Ree, M. *Nat. Mater.* **2006**, *5*, 197−203.

(20) Chang, J. F.; Sun, B.; Breiby, D. W.; Nielsen, M. M.; Sölling, T. I.; Giles, M.; McCulloch, I.; Sirringhaus, H. *Chem. Mater.* **2004**, *16*, 4772−4776.

(21) Yang, H.; Shin, T. J.; Yang, L.; Cho, K.; Ryu, C. Y.; Bao, Z. *Adv. Funct. Mater.* **2005**, *15*, 671−676.

(22) Malik, S.; Nandi, A. K. *J. Polym. Sci., Part B: Polym. Phys.* **2002**, *40*, 2073−2085.

(23) Pascui, O. F.; Lohwasser, R.; Sommer, M.; Thelakkat, M.; Thurn-Albrecht, T.; Saalwächter, K. *Macromolecules* **2010**, *43*, 9401−9410.

(24) Kim, J.-S.; Kim, J.-H.; Lee, W.; Yu, H.; Kim, H. J.; Song, I.; Shin, M.; Oh, J. H.; Jeong, U.; Kim, T.-S.; Kim, B. J. *Macromolecules* **2015**, *48*, 4339−4346.

(25) Zhang, X.; Bronstein, H.; Kronemeijer, A. J.; Smith, J.; Kim, Y.; Kline, R. J.; Richter, L. J.; Anthopoulos, T. D.; Sirringhaus, H.; Song, K.; Heeney, M.; Zhang, W.; McCulloch, I.; DeLongchamp, D. M. *Nat. Commun.* **2013**, *4*, 2238.

(26) Venkateshvaran, D.; Nikolka, M.; Sadhanala, A.; Lemaur, V.; Zelazny, M.; Kepa, M.; Hurhangee, M.; Kronemeijer, A. J.; Pecunia, V.; Nasrallah, I.; Romanov, I.; Broch, K.; McCulloch, I.; Emin, D.; Olivier, Y.; Cornil, J.; Beljonne, D.; Sirringhaus, H. *Nature* **2014**, *515*, 384−388.

(27) Lan, Y.-K.; Yang, C. H.; Yang, H.-C. *Polym. Int.* **2010**, *59*, 16−21.

(28) Salleo, A. *Mater. Today* **2007**, *10*, 38−45.

(29) Noriega, R.; Rivnay, J.; Vandewal, K.; Koch, F. P.; Stingelin, N.; Smith, P.; Toney, M. F.; Salleo, A. *Nat. Mater.* **2013**, *12*, 1038−1044.

(30) Mei, J.; Bao, Z. *Chem. Mater.* **2014**, *26*, 604−615.

(31) Babel, A.; Jenekhe, S. A. *J. Phys. Chem. B* **2003**, *107*, 1749−1754.

(32) Song, I. Y.; Kim, J.; Im, M. J.; Moon, B. J.; Park, T. *Macromolecules* **2012**, *45*, 5058−5068.

(33) Hardeman, T.; Koeckelberghs, G. *Macromolecules* **2014**, *47*, 8618−8624.

(34) Meille, S. V.; Romita, V.; Caronna, T.; Lovinger, A. J.; Catellani, M.; Belobrzeckaja, L. *Macromolecules* **1997**, *30*, 7898−7905.

(35) Trznadel, M.; Pron, A.; Zagorska, M.; Chrzaszcz, R.; Pielichowski, J. *Macromolecules* **1998**, *31*, 5051−5058.

(36) Kline, R. J.; McGehee, M. D.; Kadnikova, E. N.; Liu, J.; Fréchet, J. M. J. *Adv. Mater.* **2003**, *15*, 1519−1522.

(37) Zen, A.; Pflaum, J.; Hirschmann, S.; Zhuang, W.; Jaiser, F.; Asawapirom, U.; Rabe, J. P.; Scherf, U.; Neher, D. *Adv. Funct. Mater.* **2004**, *14*, 757−764.

(38) Kline, R. J.; McGehee, M. D.; Kadnikova, E. N.; Liu, J.; Fréchet, J. M. J.; Toney, M. F. *Macromolecules* **2005**, *38*, 3312−3319.

(39) Babel, A.; Jenekhe, S. A. *Synth. Met.* **2005**, *148*, 169−173.

(40) Park, Y. D.; Kim, D. H.; Jang, Y.; Cho, J. H.; Hwang, M.; Lee, H. S.; Lim, J. A.; Cho, K. *Org. Electron.* **2006**, *7*, 514−520.

(41) Ko, S.; Hoke, E. T.; Pandey, L.; Hong, S.; Mondal, R.; Risko, C.; Yi, Y.; Noriega, R.; McGehee, M. D.; Bredas, J. L.; Salleo, A.; Bao, Z. *J. Am. Chem. Soc.* **2012**, *134*, 5222−5232.

(42) Sivula, K.; Luscombe, C. K.; Thompson, B. C.; Fréchet, J. M. J. *J. Am. Chem. Soc.* **2006**, *128*, 13988−13989.

(43) Woo, C. H.; Thompson, B. C.; Kim, B. J.; Toney, M. F.; Fréchet, J. M. J. *J. Am. Chem. Soc.* **2008**, *130*, 16324−16329.

(44) Kanai, K.; Miyazaki, T.; Suzuki, H.; Inaba, M.; Ouchi, Y.; Seki, K. *Phys. Chem. Chem. Phys.* **2010**, *12*, 273−282.

(45) Fei, Z.; Boufflet, P.; Wood, S.; Wade, J.; Moriarty, J.; Gann, E.; Ratcliff, E. L.; McNeill, C. R.; Sirringhaus, H.; Kim, J. S.; Heeney, M. *J. Am. Chem. Soc.* **2015**, *137*, 6866−6879.

(46) Kim, J.; Song, I. Y.; Park, T. *Chem. Commun.* **2011**, *47*, 4697−4699.

(47) Chen, T. A.; Rieke, R. D. *J. Am. Chem. Soc.* **1992**, *114*, 10087−10088.

(48) Benniston, A. C.; Copley, G.; Harriman, A.; Ryan, R. *J. Mater. Chem.* **2011**, *21*, 2601−2608.

(49) Lima, C. F.; Costa, J. C.; Galvão, T. L.; Tavares, H. R.; Silva, A. M.; Santos, L. M. *Phys. Chem. Chem. Phys.* **2014**, *16*, 14761−14770.

(50) Qiao, Y.; Islam, M. S.; Han, K.; Leonhardt, E.; Zhang, J.; Wang, Q.; Ploehn, H. J.; Tang, C. *Adv. Funct. Mater.* **2013**, *23*, 5638−5646.

(51) Kim, B. J.; Lee, H.-S.; Lee, J. L.; Cho, S.; Kim, H.; Son, H. J.; Kim, H.; Ko, M. J.; Park, S.; Kang, M. S.; et al. *J. Phys. Chem. C* **2013**, *117*, 11479−11486.

(52) Donley, C. L.; Zaumseil, J.; Andreasen, J. W.; Nielsen, M. M.; Sirringhaus, H.; Friend, R. H.; Kim, J.-S. *J. Am. Chem. Soc.* **2005**, *127*, 12890−12899.

(53) Spano, F. C.; Silva, C. *Annu. Rev. Phys. Chem.* **2014**, *65*, 477−500.

(54) Yap, B. K.; Xia, R.; Campoy-Quiles, M.; Stavrinou, P. N.; Bradley, D. D. *Nat. Mater.* **2008**, *7*, 376−380.

(55) Jang, M.; Park, J. H.; Im, S.; Kim, S. H.; Yang, H. *Adv. Mater.* **2014**, *26*, 288−292.

(56) Mathijssen, S. G.; Spijkman, M. J.; Andringa, A. M.; van Hal, P. A.; McCulloch, I.; Kemerink, M.; Janssen, R. A.; de Leeuw, D. M. *Adv. Mater.* **2010**, *22*, 5105−5109.

(57) Choi, D.; Jin, S.; Lee, Y.; Kim, S. H.; Chung, D. S.; Hong, K.; Yang, C.; Jung, J.; Kim, J. K.; Ree, M.; Park, C. E. *ACS Appl. Mater. Interfaces* **2010**, *2*, 48−53.

(58) Vissenberg, M. C. J. M.; Matters, M. *Phys. Rev. B: Condens. Matter Mater. Phys.* **1998**, *57*, 12964−12967.

(59) Street, R. A.; Northrup, J. E.; Salleo, A. *Phys. Rev. B: Condens. Matter Mater. Phys.* **2005**, *71*, 165202.

(60) Mei, J.; Kim, D. H.; Ayzner, A. L.; Toney, M. F.; Bao, Z. *J. Am. Chem. Soc.* **2011**, *133*, 20130−20133.

(61) McCulloch, I.; Heeney, M.; Chabinyc, M. L.; DeLongchamp, D.; Kline, R. J.; Cölle, M.; Duffy, W.; Fischer, D.; Gundlach, D.; Hamadani, B.; Hamilton, R.; Richter, L.; Salleo, A.; Shkunov, M.; Sparrowe, D.; Tierney, S.; Zhang, W. *Adv. Mater.* **2009**, *21*, 1091−1109.

(62) DeLongchamp, D. M.; Kline, R. J.; Lin, E. K.; Fischer, D. A.; Richter, L. J.; Lucas, L. A.; Heeney, M.; McCulloch, I.; Northrup, J. E. *Adv. Mater.* **2007**, *19*, 833−837.

(63) Jang, M.; Kim, S. H.; Lee, H.-K.; Kim, Y.-H.; Yang, H. *Adv. Funct. Mater.* **2015**, *25*, 3833−3839.

(64) Beaujuge, P. M.; Fréchet, J. M. *J. Am. Chem. Soc.* **2011**, *133*, 20009−200029.